Applied Surface Science 505 (2020) 144393

Contents lists available at ScienceDirect

Applied Surface Science

journal homepage: www.elsevier.com/locate/apsusc

Full Length Article

# Deposition and characterization of a sol-gel Mg-substituted fluorapatite coating with new stoichiometries

J.M. Ferreira Jr.[a,d,*], V. Rajendran[b], G. Simonelli[a], A.C.M. Silva[a], L.C.L. Santos[a], S. Mattedi[a], L.A.M. Pontes[a], I. Costa[c], J.L. Rossi[c], M.A. Baker[b]

[a] Federal University of Bahia, Postgraduate Program of Chemical Engineering, Rua Aristides Novis, nº 02, 2º andar, Federação, Salvador, Bahia CEP 40210-630, Brazil
[b] University of Surrey, Department of Mechanical Engineering Sciences, room office 10AB03, Guildford, Surrey GU2 7XH, United Kingdom
[c] University of Sao Paulo, Nuclear and Energy Research Institute (IPEN - CNEN/SP), Av. Prof. Lineu Prestes, 2242 - Butantã, São Paulo, SP 05508-000, Brazil
[d] University of Salvador (UNIFACS), R. Dr. José Peroba, 251 - Stiep, Salvador, BA 41770-235, Brazil

ARTICLE INFO

*Keywords:*
Implant
Magnesium
Coating
Fluorapatite
Hydroxyapatite
Sol-gel
Corrosion

ABSTRACT

The calcium substitution for magnesium on fluorapatite is attractive because this element is a natural substitute in biological apatites. There are several published stoichiometries for calcium substituted by magnesium fluorapatites and most works point out that the formation and fixation of biomimetic Ca-P coatings in Ringer's solution were strongly related to $Mg^{2+}$ content and furthermore the Mg replacement improves the bioactivity of apatite. In the present study, fluorapatite (FA) and fluorapatite substituted with 6% and 7% of magnesium were obtained by deposition via sol-gel coating on substrates of AISI 316L stainless steel to investigate the effect of magnesium substitution on fluorapatite with not yet investigated stoichiometry. Characterization of coating thickness, chemical composition and crystalline structure was performed using scanning electron microscopy (SEM), X-ray photoelectron spectroscopy (XPS) and X-ray diffraction (XRD). The coating adhesion was evaluated using the pull-out test and the corrosion resistance was undertaken using potentiodynamic polarization and electrochemical impedance spectroscopy (EIS). The electrochemical results showed improvement in the corrosion resistance of magnesium-fluorapatite compared to fluorapatite coated on AISI 316L stainless steel substrates. The improvement corrosion protection and adhesion performance indicate that such magnesium fluorapatites coatings are very interesting candidates as bioactive coatings for implants.

## 1. Introduction

Metal alloys have been widely used for orthopaedic implants, due their good combination of mechanical properties [1]. The alloys of titanium, cobalt and stainless steels (SS) exhibit high strength but show varying corrosion rates when exposed to physiological mediums for long periods of time [2]. The corrosion of AISI 316L SS implants causes the formation of toxic products to osteogenic cells and together with bacterial adhesion to medical devices pose a serious problem to human health [3–5]. These toxic products disrupt the behaviour of bone marrow cells, similar to osteoblasts, which affect the proliferation and differentiation of these cells. The allergenic effects of elements released by corrosion of AISI 316L SS, such as nickel, cobalt and mainly chromium, have been reported [6–8]. Consequently, corrosion of these implants after surgery causes inflammatory responses, needing their periodic replacement, which in turn makes the implant use more expensive and compromises patient health. However, the AISI 316L SS is widely used in human implants and they can be protected by bioactive ceramic coatings, thus offering good long-term corrosion resistance and hindering the release of toxic species in the human body [5–7].

In addition to improving the corrosion resistance, bioactive ceramic coatings increase the bioactivity with faster and more efficient osseointegration [9]. Calcium phosphates, dense alumina ($Al_2O_3$), titanium dioxide ($TiO_2$), and silica/calcium phosphate, apatites and hydroxyapatite ceramics are widely used as bioceramics [10–13]. Hydroxyapatite (HA), $Ca_{10}(PO_4)_6OH_2$ is a compound which represents the mineral phase of bones and teeth, responsible for providing structural stability to the body and functioning as an ion buffer reservoir. HA is the most used bioceramic implant coating, with similar chemical composition to the inorganic matrix of the skeleton allows stabilization

* Corresponding author at: Federal University of Bahia, Postgraduate Program of Chemical Engineering, Rua Aristides Novis, nº 02, 2º andar, Federação, Salvador, Bahia CEP 40210-630, Brazil

*E-mail addresses:* jmfj@ufb.br (J.M. Ferreira), gsimonelli@ufba.br (G. Simonelli), acristinasilva@ufba.br (A.C.M. Silva), lclsantos@ufba.br (L.C.L. Santos), uolpontes@uol.com.br (L.A.M. Pontes), icosta@ipen.br (I. Costa), jelrossi@ipen.br (J.L. Rossi), m.baker@surrey.ac.uk (M.A. Baker).

https://doi.org/10.1016/j.apsusc.2019.144393
Received 9 September 2019; Received in revised form 9 October 2019; Accepted 12 October 2019
Available online 25 October 2019
0169-4332/ 

of the implant, reducing the cure time and adhesion to the prosthesis [14–18]. Several beneficial factors, such as its morphology, biocompatibility, adhesion and corrosion resistance has led to the extensive use of HA as a bioactive ceramic coating for various polymeric and metallic substrates used in biomedical applications [19]. However, even with these favourable properties, the use of synthetic HA is still limited due to its poor mechanical properties.

HA can be synthesized by different methods, such as hydrothermal method, plasma spraying method, sputtering process, biomimetic method, electrochemical deposition and the sol-gel method [18–26]. Among the different methods of synthesis and deposition of bioactive ceramic coatings, the sol-gel deposition has many advantages, including coating uniformity, conformal coverage of the component and good control of composition and thickness.

The bioactivity, biocompatibility, solubility and adsorption properties of HA can be altered and even controlled by ionic substitution. Research works have shown that the substitution of hydroxyl ($OH^-$) groups in hydroxyapatite for fluorine ($Ca_{10}(PO_4)_6(OH)_xF_{2-x}$) forming fluorapatite (FA), $Ca_{10}(PO_4)_6F_2$, promotes an improvement in mechanical properties, adhesion, and compressive strength [27,28]. Another particularly important factor is that fluorinated bioceramics stimulate the proliferation of bone cells and their differentiation. As a result, FA is used as an alternative to HA for biomedical implant applications [28–30].

The search for new and better materials has led to consideration of substituting calcium with magnesium in the FA structure, ($Ca_{10-x}Mg_x(PO_4)_6F_2$) to form Mg fluorapatite (MgFA). Mg is the fourth most abundant mineral in the body, after calcium, potassium, and sodium, with approximately 40% being intracellular and the rest being present in the bone or teeth. Magnesium is one of the essential elements for all living organisms with more than 100 enzymes using this element for catalytic purposes [31–34]. In addition, Mg is naturally replaced into biological apatites in the human body. Mg-substituted HA increased the cell number, alkaline phosphatase activity and osteocalcin secretions suggesting that content of Mg-substituted could improve implant osseointegration in the early stages of bone healing compared with pure HA. One might expect that Mg-substituted on FA would also have similar positive effects [4,34].

The present study builds on the investigation of the corrosion resistance of Mg fluorapatite (MgFA) coated AISI 316L substrates in Ringer's solution for two intermediate stoichiometry 6% and 7% at% (MgFA6 and MgFA7 specimens) Mg-substituted on the fluoroapatite, in terms of the morphology of the coating, the microstructure, the homogeneity and thickness, the composition before and after corrosion and the coating adhesion to the substrate.

## 2. Materials and methods

AISI 316L SS discs (24 mm diameter and 2 mm thick) were mechanically polished successively with SiC papers (grit size: P320, P600, P1200 and P4000). The substrates were subsequently sonicated in ethanol, acetone and distilled water (each bath for 15 min) before being dried in an oven for 15 min at 60 °C.

The sol-gel solution was prepared using phosphorous pentoxide, calcium nitrate tetrahydrate, and magnesium nitrate hexahydrate supplied by Sigma-Aldrich. Initially, the phosphorous pentoxide was dissolved in absolute ethanol (forming a P solution). Separately, either calcium nitrate tetrahydrate for FA or calcium nitrate tetrahydrate and magnesium nitrate for MgFA were dissolved in absolute ethanol hexahydrate, forming a Ca or Ca-Mg solution [4]. The Ca or Ca-Mg solution was added dropwise to the P solution. A previously determined volume of hexafluorophosphoric acid was added to the Ca-P or Ca-Mg-P solution. The amounts of chemical precursors previously listed were used in order to obtain a coating with 6% and 7% of Mg substituted in the fluorapatite. The samples were prepared according to the ratio between elements presented in the literature to FA samples Ca/P = 1.67, MgFA6 samples Ca + Mg/P = 1.67 and MgFA7 samples Ca + Mg/P = 1.67 for samples substituted by Mg ratio Ca/F = 5 [4]. The solution was then magnetically stirred at room temperature for 24 h in a sealed beaker to prevent any evaporation and gelation of the solution. The AISI 316L SS samples were vertically dipped into the sol-gel solution at a rate of 1 mm·sec$^{-1}$. The samples were then left to age for 24 h at room temperature before being dried in an oven at 60 °C for 24 h. Finally, the samples were calcined at a rate of 1 °C·min$^{-1}$ up to 600 °C for 15 min in a muffle furnace and then slowly cooled to room temperature in the furnace, using the same rate as employed for heating [4]. The samples of AISI 316L SS and FA coated AISI 316L SS were prepared and tested to compare their results with those of MgFA coated AISI 316L SS samples.

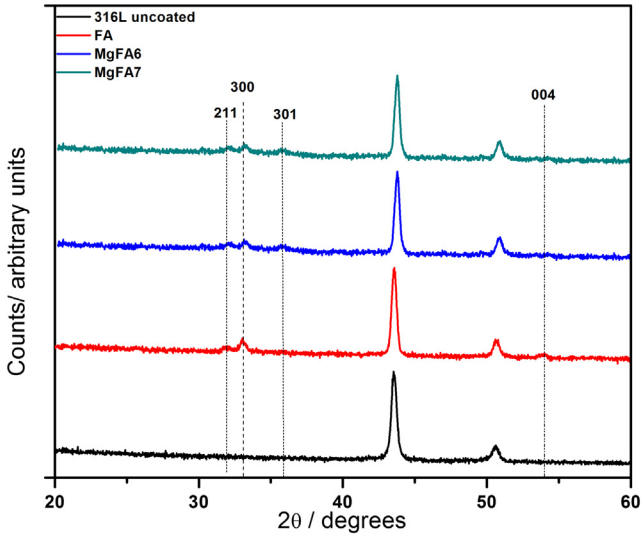


**Fig. 1.** GAXRD diffractograms for the AISI 316L SS substrate, coated with fluorapatite FA, 6% at. Mg-substituted FA (MgFA6) and 7% at. Mg-substituted FA (MgFA7).

The coating morphology and thickness were examined and measured using a scanning electron microscope (SEM), employing a Schottky field emission gun, operated at an incident voltage of 15 keV.

The chemical composition surface was determined by X-ray photoelectron spectroscopy (XPS) carried out employing a monochromated Al $K_\alpha$ source (operated at 15 kV and 20 mA) and a 400 μm spot size. XPS survey spectra were acquired at an analyser pass energy of 100 eV. The core level spectra were recorded at a pass energy of 50 eV and 0.2 eV step size. Charge compensation was achieved using a low-energy electron flood gun and spectra were charge was corrected to the adventitious carbon peak at 285.0 eV. The quantification was performed following the removal of the Shirley background and use of instrument modified Wagner sensitivity factors. The glancing angle X-Ray diffraction (GAXRD) was performed on an instrument using a Cu$K_\alpha$ radiation source with a 1° incident angle and a diffraction angle (2θ) in the range of 10–70°. The crystallinity degree was calculated use of two-phase model, i. e. the samples are composed of crystalline and amorphous regions, using Eq. (1):

$$Xc = I_{crystalline} * (I_{crystalline} + I_{amorphous})^{-1} \quad (1)$$

The pull-out adhesion tests were performed in a tensile test machine with a 1 kN load cell and controlled by the manufacturer's software. The contact pin had a bottom face contact area of 19.6 mm$^2$ and a cyanoacrylate adhesive was employed to adhere the pin to the coating surface.

The corrosion properties of coatings were investigated using a three electrode cell arrangement with an Ag/AgCl, KCl saturated electrode and a platinum wire as the reference and counter electrodes, respectively. A potentiostat and software was employed to record open circuit potential (OCP) variation with time of test, the potentiodynamic

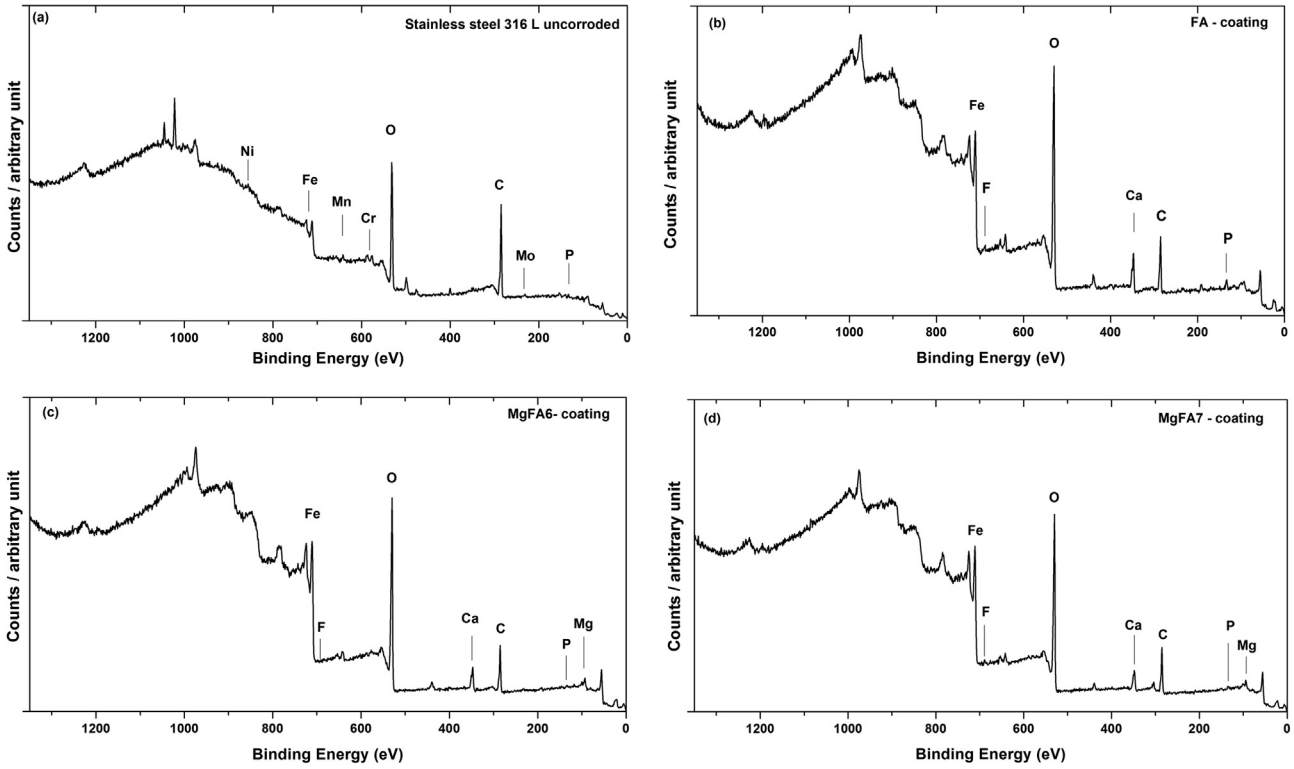


**Fig. 2.** XPS Survey spectra to: (a) stainless steel AISI 316 L, (b) fluorapatite (FA), (c) 6% at. Mg-substituted FA (MgFA6) and (d) 7% at. Mg-substituted FA (MgFA7).

**Table 1**
Atomic concentration obtained by XPS to samples 316 L, FA, MgFA6 and MgFA7.

| Peak | AISI 316 L | FA | MgFA6 | MgFA7 |
|---|---|---|---|---|
| | at.% | | | |
| C 1s | 10.10 | 6.00 | 8.00 | 3.20 |
| Ca 2p | 0.00 | 7.40 | 5.80 | 4.10 |
| Mg 1s | 0.00 | 0.00 | 2.31 | 4.40 |
| P 2p | 0.00 | 7.30 | 6.67 | 4.10 |
| O 1s | 54.00 | 63.60 | 60.89 | 62.50 |
| F 1s | 0.00 | 0.98 | 0.93 | 0.81 |
| Fe 2p | 8.90 | 10.40 | 11.40 | 16.60 |
| Mn 2p | 2.70 | 2.20 | 1.50 | 1.80 |
| Cr 2p | 6.80 | 0.12 | 0.70 | 0.50 |
| Mo 3d | 1.50 | 0.40 | 0.40 | 0.39 |
| Ni 2p | 4.50 | 1.60 | 1.40 | 1.60 |
| S 2p | 1.50 | – | – | – |
| Si 2p | 10.00 | – | – | – |

polarization curves and electrochemical impedance spectroscopy (EIS) measurements. A surface area of 1 $cm^2$ was exposed in Ringer's solution as the corrosive medium at room temperature (25 °C). The Ringer strength tablets supplied by Sigma-Aldrich composed of calcium chloride (0.120 $g{\cdot}L^{-1}$), potassium chloride (0.105 $g{\cdot}L^{-1}$), sodium bicarbonate (0.050 $g.L^{-1}$) and sodium chloride (2.250 $g{\cdot}L^{-1}$) was used to prepare a Ringer's test solution at room temperature, it closely replicates the natural body solution.

EIS tests were performed in frequency range from 100 kHz to 10 mHz, with a signal amplitude perturbation of 10 mV and data acquisition rate of 10 points per decade. The acquisition occurred in consecutive loops at 5 h intervals for both EIS and potentiodynamic polarization. The potentiodynamic polarization curves were recorded in the sweep range ± 200 mV versus OCP with a scan rate of 1.667 $mV{\cdot}s^{-1}$. The impedance results were used as reference for the protection against corrosion by the deposited coatings. Although most studies on corrosion protection effects of fluoropatites and fluoropatites substituted with magnesium are carried out in Ringer's solution at body temperature and for long periods of time, this work was performed with Ringer's solution at room temperature and for 100 h as the first approach in the search of information about the potentiality of the two new stoichiometries between 5% and 10% of Mg substituted on fluoroapatite.

The immersion test for weight loss monitoring was performed for samples AISI 316 L, FA, MgFA6 and MgFA7. The procedure consisted of cleaning the samples ultrasonically in deionized water and immersing for a predetermined period of time in 10 $mL{\cdot}cm^{-2}$ of Ringer's solution. Sequentially the samples were carefully removed, washed in deionized water and dried at room temperature. The weight loss calculation involved the mass values obtained by weighing the samples before and after the immersion process in Ringer's solution using a analytical balance with precision of 0.01 mg. The data were used to calculate the corrosion rate according to Eq. (2).

$$C_R = K(WA^{-1}d^{-1}t^{-1}) \quad (2)$$

where the corrosion rate is $C_R$ ($mm{\cdot}year^{-1}$), K is a constant with value of $8.76 \times 10^4$, the weight loss is W (g), the total surface area exposed to solution is A ($cm^2$), the density of substrate is d ($g{\cdot}cm^{-3}$) and exposure time is t (h).

## 3. Results and discussion

Three replicate tests for each condition were performed and the results shown are representative of these specimens (XPS, SEM/FEG, XRD and EIS) and in some cases are the arithmetic average of the results obtained (adhesion test and corrosion rate).

Fig. 1 shows the XRD patterns of the AISI 316L SS substrate uncoated, together with FA, MgFA6 and MgFA7 coated substrates. It is possible to observe that increasing the content of Mg on MgFA6 and MgFA7 peaks shifted slightly to higher angles. The shift is due to the ionic radius of $Mg^{2+}$ which is smaller than that of $Ca^{2+}$, 0.78 Å and 0.106 Å, respectively. The shift of the XRD peaks with respect to the FA (ICDD ref no. 00-003-0732), serves as evidence of Mg substitution in

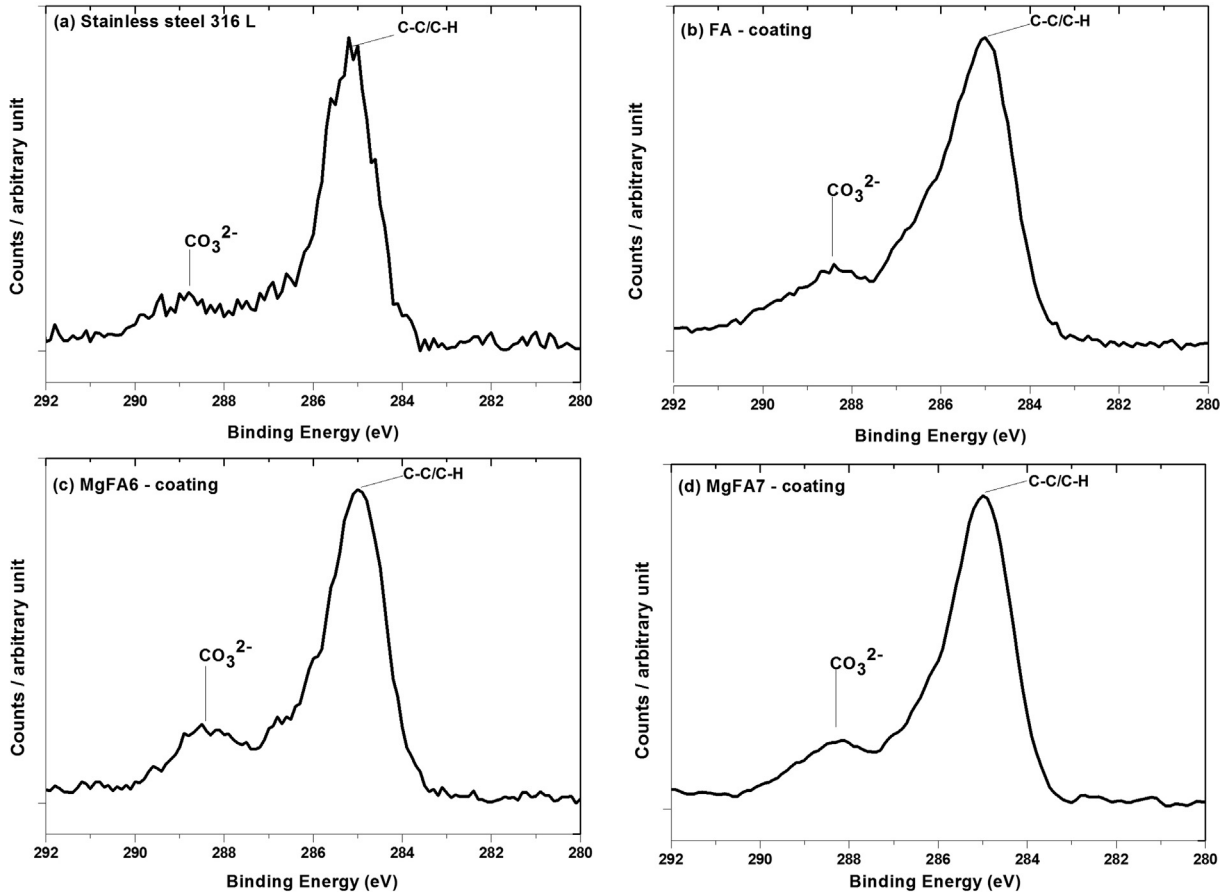


**Fig. 3.** XPS high resolution spectra to (a) stainless steel AISI 316 L, (b) fluorapatite (FA), (c) 6% at. Mg-substituted FA (MgFA6) and (d) 7% at. Mg-substituted FA (MgFA7).

**Table 2**
Atomic concentration obtained by XPS to samples FA, MgFA6 and MgFA7.

| Peak | FA | MgFA6 | MgFA7 |
|---|---|---|---|
| | at.% | | |
| Ca 2p | 24.38 | 25.90 | 27.70 |
| O 1s | 56.67 | 54.00 | 50.80 |
| P 2p | 14.60 | 14.10 | 14.80 |
| Mg 1s | – | 1.40 | 1.80 |
| F 1s | 4.35 | 4.60 | 4.90 |

**Table 3**
Theoretical and observed experimental values of Ratio Ca/P to FA coating and MgFA coatings.

| Ratio | Theoretical | FA | MgFA6 | MgFA7 |
|---|---|---|---|---|
| Ca/P | 1.67 | 1.65 | 1.83 | 1.82 |
| Ca + Mg/P | 1.67 | – | 1.67 | 1.67 |
| Ca/F | 5.00 | 5.60 | 5.63 | 5.65 |

the prepared coatings.

In addition to the substrate peaks, the pure FA and MgFA coatings show small FA peaks corresponding to (2 1 1), (3 0 0), (0 0 4) and (2 1 1), (3 0 0), (3 0 1) and (0 0 4) reflections, respectively (ICDD ref no. 00–003-0732). These results indicate that coatings FA, MgFA6 and MgFA7 are nanocrystalline. The XRD data allowed the calculation of the values of the degree of crystallinity (Eq. (1)) 78.5%, 65% and 59% respectively for samples FA, MgFA6 and MgFA7. The decrease in crystallinity with addition and increase of Mg in fluorapatites can be attributed to TCP formation, a similar effect has already been reported for Mg-substituted hydroxyapatites [7,8].

Three kinds of specimens were prepared according to the following composition: $Ca_{10-x}Mg_x(PO_4)_6F_2$, the substitution determined by the × letter and the values where x = 0, x = 0.6 and × = 0.7, respectively for samples FA, MgFA6 and MgFA7.

The composition of surface was investigated by X-ray photoelectron spectroscopy (XPS). The results for AISI 316 L stainless steel, fluorapatite (FA), 6% Mg-substituted FA (MgFA6) and 7% Mg- substituted FA (MgFA7) are shown in Fig. 2.

The AISI 316L stainless steel after polishing and ultrasonic cleaning in organic solvents and water was oven dried at 80 °C for 10 min and immediately taken to the XPS. Even with such care the results showed high contamination by hydrocarbons. The presence of AISI 316 L alloy elements shows that the coating is not uniform, with areas of the substrate exposed to XPS analysis (5 nm). Table 1 shows the elements presents on the XPS survey spectrum and the atomic concentrations to the AISI 316 L stainless steel, samples FA, MgFA6 and MgFA7.

The concentration values of the AISI 316L alloying elements were removed and the elements of interest Ca, Mg, P, O and F were adjusted by their high resolution XPS spectra. The XPS high resolution spectrum for carbon of the samples AISI 316 L steel, and stainless steel coatings FA, MgFA6 and MgFA7 are shown in Fig. 3.

The carbon peak can be adjusted in two peaks, the main one referring to hydrocarbon contamination and the second carbonate peak. The cleaning and drying process for the sample of AISI 316L steel is responsible for the formation of carbonate from carbon dioxide in the environment dissolved in water. Following the rules given by, it is possible to confirm that the carbon peaks present in the spectra are a result of contamination. The C 1s peak, from contamination have asymmetric shape. Also, the fact that the background slope is slightly

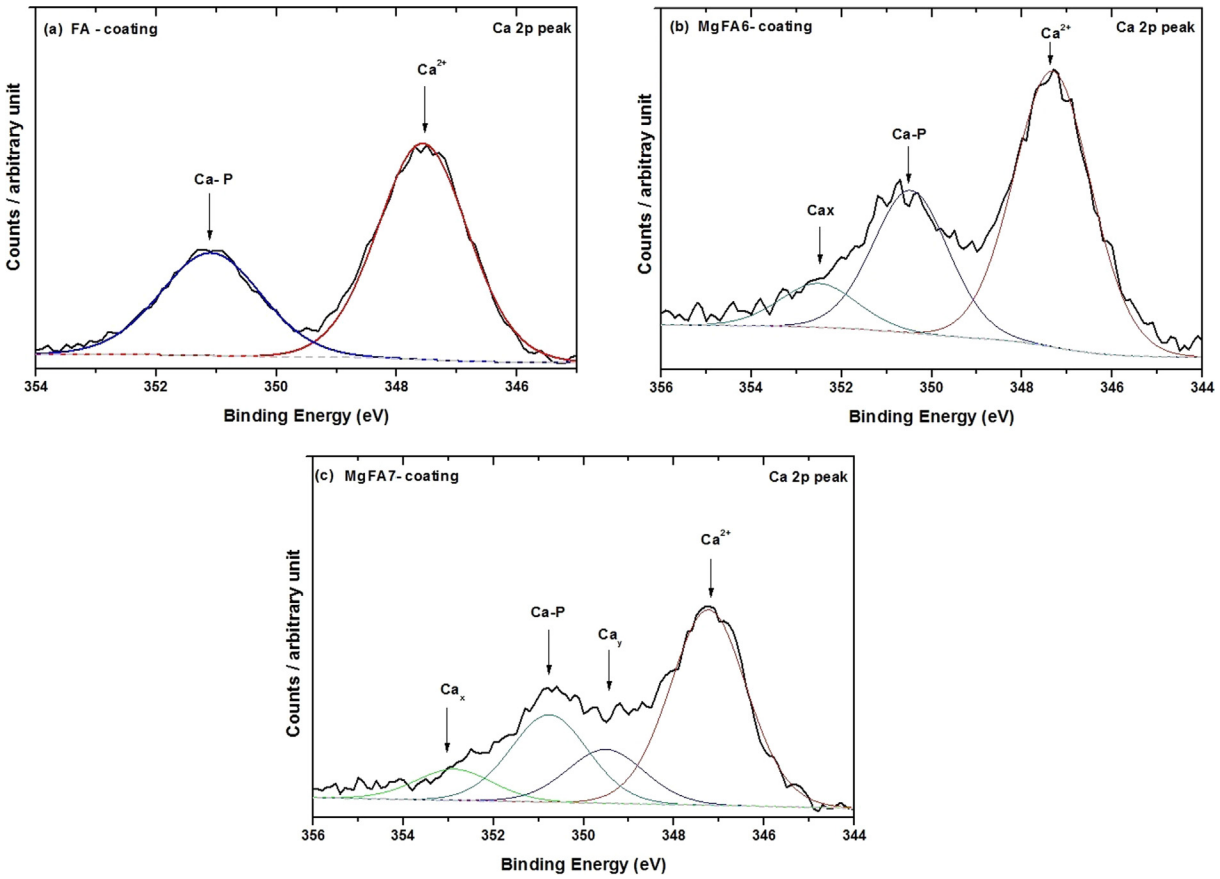


**Fig. 4.** XPS high resolution Ca2p and Ca1p spectras to (a) fluorapatite (FA), (b) 6% at. Mg-substituted FA (MgFA6) and (c) 7% at. Mg-substituted FA (MgFA7).

decreasing confirms that the peak is due to the contamination, the element carbon is in the outermost layer [35,36]. Considering the carbon as a contaminant and removing the elements from alloy substrate it is possible to obtain the concentrations of the elements of interest, referring to the coating of fluorapatite and fluorapatite substituted with magnesium. The atomic concentration values for the elements of interest are shown in Table 2.

According to the Ref. [4] it is possible to observe the stoichiometry through the relations between the elements Ca, Mg and P. For FA the ratio will be Ca/P = 1.67 and for MgFA Ca + Mg/P = 1.67, these ratios are shown in the Table 3.

The ratio among the elements shows a good agreement with the reference values, however it is possible to observe that the reference stoichiometries and the stoichiometry obtained are different due to the amount of fluorine. For the FA sample the stoichiometry found was $Ca_{10}P_{6.1}O_{23.7}F_{1.7}$, for MgFA6 was $Ca_{9.5}Mg_{0.6}P_{6.0}O_{24.8}F_{1.9}$ and for MgFA7 was $Ca_{9.0}Mg_{0.7}P_{5.8}O_{21.7}F_{1.9}$. The XPS results showed that the stoichiometry is different for the coatings FA and that the substituted magnesium shows an increase in the concentration of this element to the target values. A good procedure for the characterization of apatites is the peak XPS of calcium in high resolution due to this element presents defined peaks Ca $2p_{1/2}$ and Ca $2p_{3/2}$ for fluorapatite reported, respectively in 351.2 eV and 347.6 eV [37–39]. The XPS high resolution Ca $2p_{1/2}$ and Ca $2p_{3/2}$ spectra and oxygen (O 1s) were decomposed and the adjustments are shown, respectively in Fig. 4 and Fig. 5.

The binding energy (BE) of calcium (Ca 2p), which equals 347.6 eV, show that calcium is on the second stage of oxidation ($Ca^{2+}$) and occurs most likely as $Ca_3(PO_4)_2$ [37–39]. The high-resolution Ca 2p and P 2p spectra reveal that the Ca 2p spectrum is a doublet with Ca $2p_{3/2}$ and Ca $2p_{1/2}$ at 347.4 and 351.0 eV, respectively. The compilation of the XPS values, atomic concentration and binding energies, Ca 2p peak fitting for coatings FA, MgFA6 and MgFA7 are showed in Table 4.

The results show that the two main peaks characteristic of fluorapatite were present for all samples and that the magnesium addition (MgFA6 and MgFA7 samples) increase the number of peaks. These peaks present for samples substituted by magnesium may be related by the occupation of magnesium in the calcium sites. The high resolution spectra for O 1s and peak fitting for coatings FA, MgFA6 and MgFA7 are shown in Fig. 5.

The O 1s spectra of FA, MgFA6 and MgFA7 films contains three oxygen species: $O_2^-$, $OH^-$ and adsorbed $H_2O$ at BE values 530 ± 0.2 eV, 532 ± 0.2 eV and 534 ± 0.2 eV, respectively [37–44]. The position of these peaks is very similar in all the samples analysed, but the quantitative contribution of the oxygen species is different (Fig. 5). The main component at BE = 532 eV in samples AISI 316 L and FA can be attributed to $OH^-$ groups. For fluorapatite magnesium substituted MgFA6 and MgFA7 main component is $O_2^-$ species at BE = 530 eV, attributable to metal oxide. The O 1s spectrum is dissymmetric due to the two types of oxygen in $PO_4$ groups or M-$PO_4$ groups, O 1s peak that contains only $PO_4$ groups is symmetrical. The addition of magnesium on fluorapatite increases de contribution of $O_2^-$, and the peak with different amount of magnesium shows similar shape. The compilation of these results are shown in Table 5.

An indication of fluorapatite formation is the position of P $2p_{3/2}$ peak reported by Landis in 133.6 eV [38,39]. The high resolution XPS normalized peaks for P $2p_{3/2}$ for the coatings samples FA, MgFA6 and MgFA7 are shown in Fig. 6.

As can be observed in the XPS results in the P $2p_{3/2}$ spectra, all peaks are centered in 133.6 eV for the fluorapatite phosphate group. It is also notable that the peaks for the samples magnesium substituted fluoroapatite are wider showing that the addition of magnesium leads to a change in the chemical structure and hence change in the form of the phosphorus peak. Others factors contributing to peak broadening include strain and inhomogenities compositions. The presence of

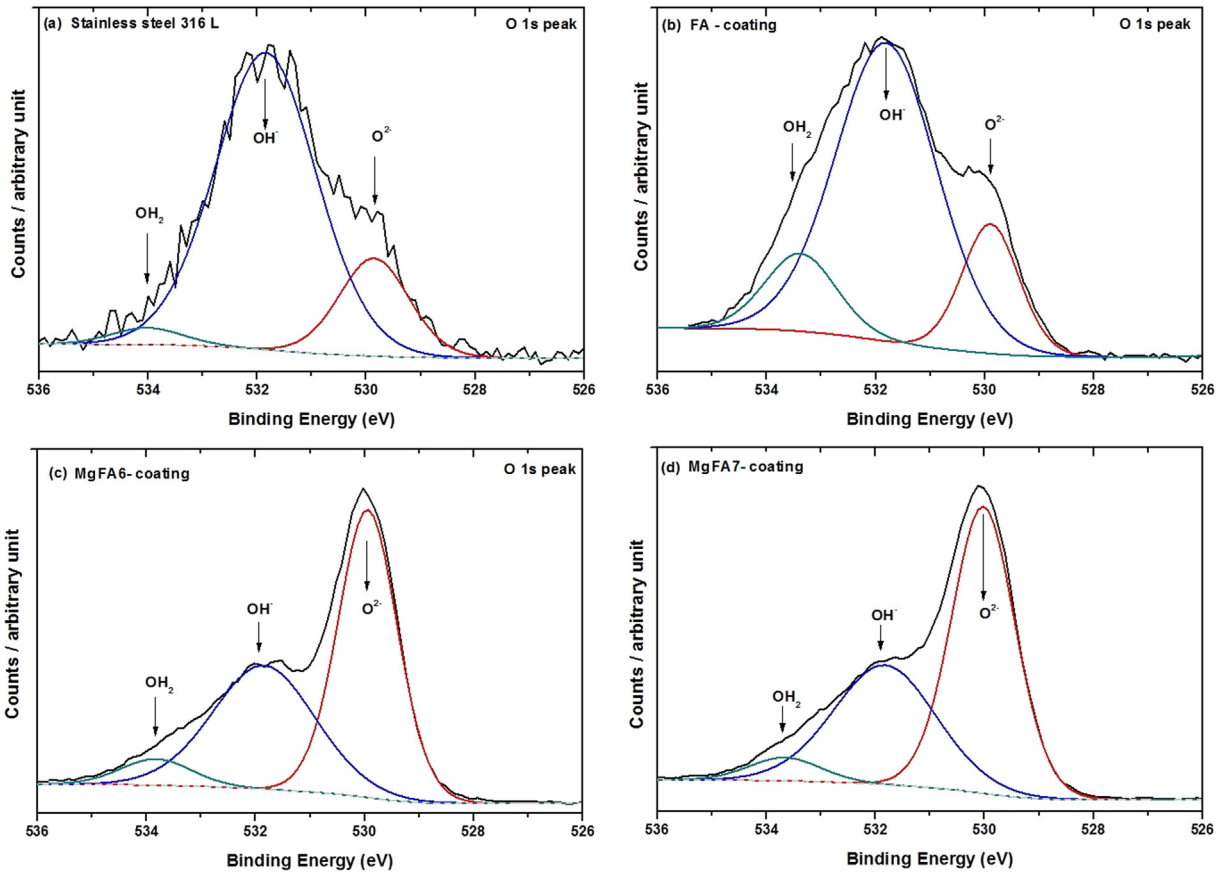


**Fig. 5.** XPS high resolution O 1s spectras for (a) stainless steel AISI 316 L, (b) fluorapatite (FA), (c) 6% at. Mg-substituted FA (MgFA6) and (d) 7% at. Mg-substituted FA (MgFA7).

**Table 4**
Atomic concentration and binding energy for samples of fluorapatite (FA), 6% at. Mg-substituted FA (MgFA6) and 7% at. Mg-substituted FA (MgFA7).

| Peak fitting | BE (eV) | FA | MgFA6 | MgFA7 |
|---|---|---|---|---|
| **at.%** | | | | |
| $Ca^{2+}$ | 347.6 ± 0.2 | 65.33 | 60.06 | 52.89 |
| $Ca_y$ | 349.5 ± 0.2 | – | 30.38 | 23.89 |
| Ca-P | 351.0 ± 0.2 | 34.67 | 9.56 | 8.50 |
| $Ca_x$ | 352.7 ± 0.3 | – | – | 14.72 |

**Table 5**
Atomic concentration and binding energy to samples 316L, FA, MgFA6 and MgFA7.

| Peak fitting | BE (eV) | AISI 316L | FA | MgFA6 | MgFA7 |
|---|---|---|---|---|---|
| | | **at.%** | | | |
| $O_2^-$ | 530.0 ± 0.2 | 17.95 | 17.04 | 54.00 | 56.69 |
| $OH^-$ | 532.0 ± 0.2 | 78.91 | 69.22 | 40.08 | 38.13 |
| $H_2O$ | 534.0 ± 0.2 | 3.14 | 13.75 | 5.92 | 5.17 |

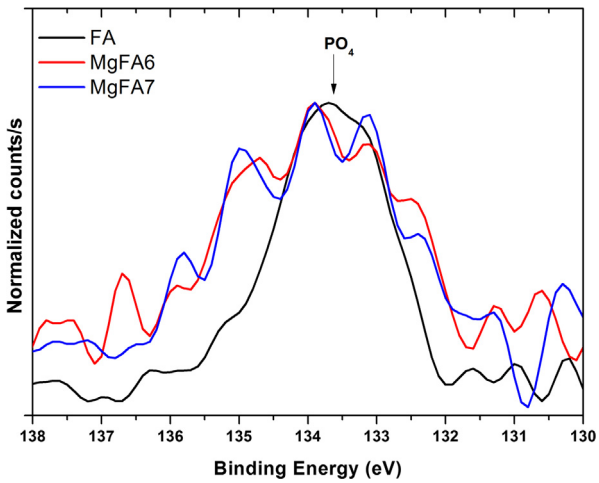


**Fig. 6.** High resolution XPS normalized peaks P $2p_{3/2}$ for coatings on samples fluorapatite (FA), 6% at. Mg-substituted FA (MgFA6) and 7% at. Mg-substituted FA (MgFA7).

fluoride in the coatings is shown by high resolution XPS normalized F 1s peaks, see Fig. 7.

From the XPS profile of samples FA, MgFA6 and MgFA7 shown similar shapes of F 1s peaks (see Fig. 7), only the F 1s profile for fluorine in hydroxy fluoroapatite phase (684.2 eV). In this way, the XPS results showed that stoichiometries are different for FA coatings and that magnesium causes an increase in the concentration of this element close to the target values. Therefore, the stoichiometries were considered achieved and the denomination of the samples initially obtained $Ca_{10}P_{6.1}O_{23.7}F_{1.7}$ (FA), $Ca_{9.5}Mg_{0.6}P_{6.0}O_{24.82}F_{1.98}$ (MgFA6) and $Mg_{0.7}P_{5.8}O_{21.7}F_{1.90}$ (MgFA7) was correctly nominated.

The Fig. 8 shows scanning electron micrographs - SEM using secondary electrons of the surface of the samples fluorapatite (FA), 6% at. Mg-substituted FA (MgFA6) and 7% at. Mg-substituted FA (MgFA7). This images point out the observation of non-cracked and uniform coatings, with a small number of defects.

According to the images it is possible to observe that the addition of Mg causes a coating densification, with a lower number of defects present in the MgFA7 sample surface. Cracks and pores are responsible

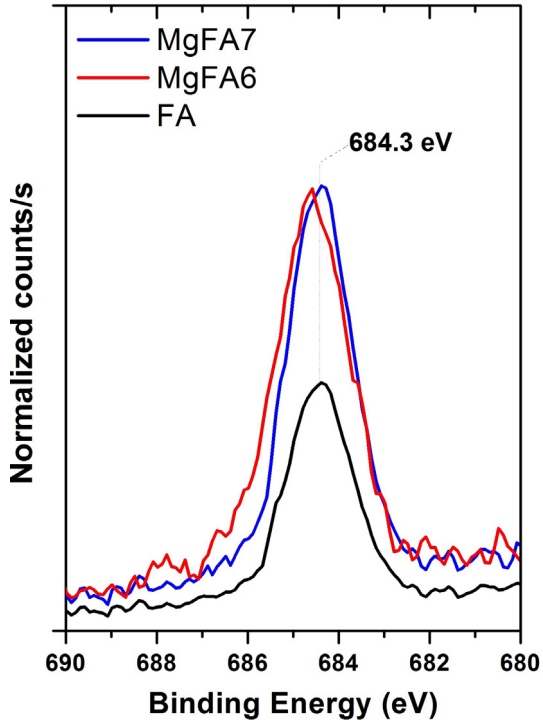


**Fig. 7.** High resolution XPS normalized peaks for F 1s for coatings on samples fluorapatite (FA), 6% at. Mg-substituted FA (MgFA6) and 7% at. Mg-substituted FA (MgFA7).

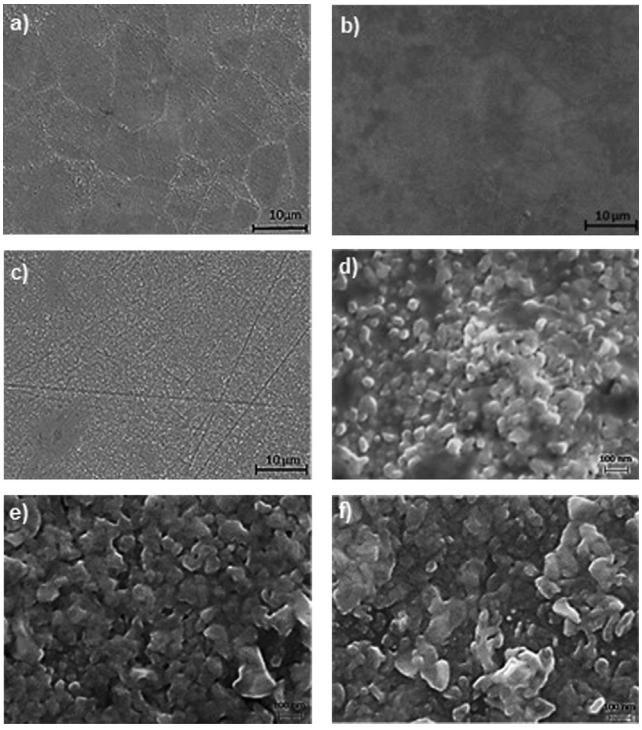


**Fig. 8.** Scanning electrom micrographs - SEM using secondary electrons of the surface of the samples fluorapatite (FA) (a, d), 6% at. Mg-substituted FA (MgFA6) (b, e) and 7% at. Mg-substituted FA (MgFA7) (c, f).

for significant effects on corrosion susceptibility in a humid and corrosive environment. Studies have shown that the corrosion rate of the different substrates after HA coating is higher than the substrate due to the presence of pores [38–42]. Defects promote the penetration of body fluid at the coating/substrate interface in a biological environment

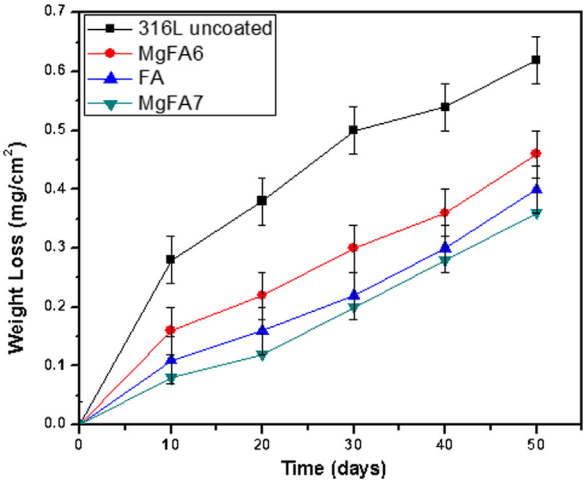


**Fig. 9.** Variations of weight loss for AISI 316 L uncoated sample, fluorapatite (FA), 6% at. Mg-substituted FA (MgFA6) and 7% at. Mg-substituted FA (MgFA7) as a function of immersion time in Ringer's solution at 25 ± 0.5 °C up to 50 days.

**Table 6**
Corrosion rate of samples 316 L uncoated, FA, MgFA6 and MgFA7 after 50 days of immersion in Ringer's solution at 25 ± 0.5 °C calculated by Eq. (2).

| Sample | Corrosion rate (mm·year$^{-1}$) |
|---|---|
| AISI 316L uncoated | $5.1 \times 10^{-3}$ |
| FA | $4.1 \times 10^{-3}$ |
| MgFA6 | $4.3 \times 10^{-3}$ |
| MgFA7 | $2.9 \times 10^{-3}$ |

changing local pH and lead a subsequent dissolution of the HA coating. The corrosion mechanism of the porous FA coating can be summarized by the production of $H^+$ ions in the interface area where corrosion occurs and then is followed by the dissolution of FA coating in the high $H^+$ concentration area, a mechanism similar to the corrosion crack mechanism [4].

Fig. 9 shows the weight loss of samples AISI 316 L uncoated, FA, MgFA6 and MgFA7 coated samples, immersed up to 50 days in Ringer's solution at 25 ± 0.5 °C where the points refer to the average weight loss and an error bar is the standard deviation of the three measurements.

It is possible to observe that AISI 316 L uncoated samples show the highest weight loss through the whole period of immersion test and samples MgFA7 the lowest weight loss, although the changes of slope for all samples is quite similar. A tendency in the increase of mass loss is observed and is due to the fact that the observation period is relatively short, with a possible increase of mass loss and corrosion rate in periods of exposure to the Ringer's solution for more than 50 days. The corrosion rates after 50 days are presented in Table 6.

The corrosion rates calculated from the immersion test are lower for the coated samples, which justifies the surface treatments. Although this test was performed at room temperature rather than at body temperature the results are indicative that the coatings are actually functional mainly the MgFA7. The weight loss results together with the calculated corrosion rates were used as a way to select the most promising treatments with respect to the corrosion protection. Therefore, the adhesion tests, electrochemical characterization (EIS and potentiodynamic polarization) and chemical characterization before corrosion (XPS) were performed only for samples FA and MgFA7.

The final set of images (Fig. 10a and b) are related to the polished cross-sections of the two coatings. The first feature that can be observed from these images is the thicknesses of the coatings. Fig. 10a for the FA

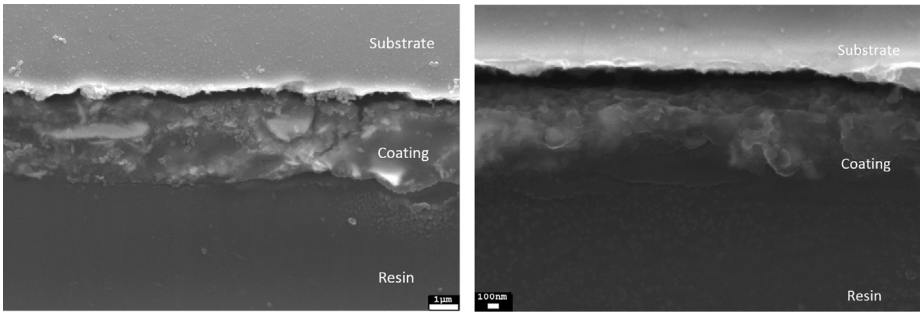


**Fig. 10.** Scanning electron micrographs using secondary electrons of: (a) fluorapatite (FA), (b) 7% at. Mg-substituted FA (MgFA7).

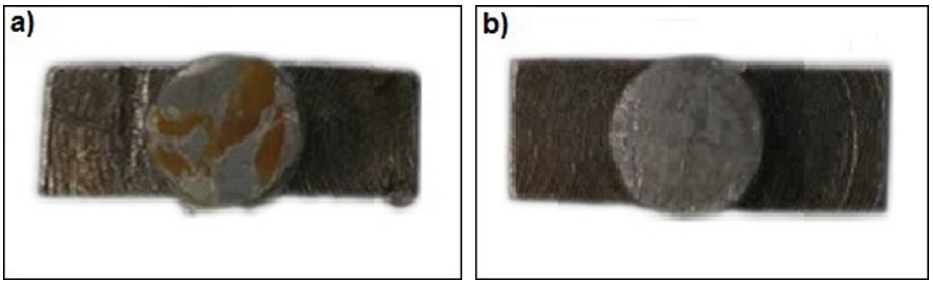


**Fig. 11.** Typical fracture surfaces for (a) fluorapatite (FA), (b) 7% at. Mg-substituted FA (MgFA7), coated following the pull-out testing.

**Table 7**
Pull-off adhesion test results for the FA coated 316L SS substrate.

| Test number | Failure load (N) | Failure limit (MPa) | Failure mode |
|---|---|---|---|
| **1** | 68.5 ± 0.2 | 3.5 ± 0.2 | Interfacial (coating/substrate) |
| **2** | 73.2 ± 0.2 | 3.7 ± 0.2 | Interfacial (coating/substrate) |
| **3** | 83.0 ± 0.2 | 4.2 ± 0.2 | Interfacial (coating/substrate) |
| **4** | 87.3 ± 0.2 | 4.5 ± 0.2 | Interfacial (coating/substrate) |
| **Mean value:** | **78.0 ± 0.2** | **4.0 ± 0.2** | |

**Table 8**
Pull-off adhesion testing results for MgFA7 coated 316L SS substrate.

| Test number | Failure load (N) | Failure limit (MPa) | Failure mode |
|---|---|---|---|
| 1 | 80.8 ± 0.2 | 4.1 ± 0.2 | Interfacial (adhesive/coating) |
| 2 | 95.8 ± 0.2 | 4.9 ± 0.2 | Interfacial (adhesive/coating) |
| 3 | 90.0 ± 0.2 | 4.6 ± 0.2 | Interfacial (adhesive/coating) |
| 4 | 86.4 ± 0.2 | 4.4 ± 0.2 | Interfacial (adhesive/coating) |
| **Mean value:** | **88.3 ± 0.2** | **4.5 ± 0.2** | |

coating was taken and the resulting coating thickness was measured as 3 μm. Fig. 10b for the MgFA7 meanwhile, was captured at higher magnification with the coating thickness measured to be approximately 1.0 μm. Similar studies based on hydroxyapatite coatings show that a thinner coating tends not to display delamination during fatigue or final fracture however both coatings are within that “thin” category, so the difference in this case may be negligible. Interestingly, both coatings are much thinner than those achieved in other studies such as by Sharifnabi et al., in 2014, who achieved thicknesses of 10 μm for a 10% MgFA coating on the same substrate material [4]. One key benefits of a thinner coating as found by Aksakal et al., in 2010 [45,46] it is the improved bonding network in the ceramic material. Another advantage is that the thinner the coating is, the lower the amount of expected surface cracks, which means that there is a lower tendency for implant loosening concurrency. Surface cracks have been proven to be detrimental to the corrosion resistance of the coating and is the indirect reason why thinner coatings typically display better corrosion resistance in practice than thicker coatings, contrary to what might be expected [45].

Another aspect that follows on from this is the variation in the coating thickness. As it can be observed from Fig. 10a, the FA coating thickness remains relatively consistent with a clear outer edge being displayed. This contrasts with the MgFA7 coating in Fig. 10b in which the thickness of the coating varies from left to right. It could be argued that this observation is simply an anomaly of one point in the cross-section but the same trend was observed across multiple points with the FA coating thickness repeatedly remaining more stable than its MgFA7 counterpart.

Two main factors should be taken into account when investigating the protective properties of a layer, the barrier effect related to layer thickness and capacitance of this layer. Coatings with similar thickness values, allow eliminating the barrier effect and assigning corrosion protection to the different surface morphologies and their chemical properties.

Inspection of the fracture surface showed that failure occurred at different locations in the pin joint for the FA and MgFA7 coatings, as

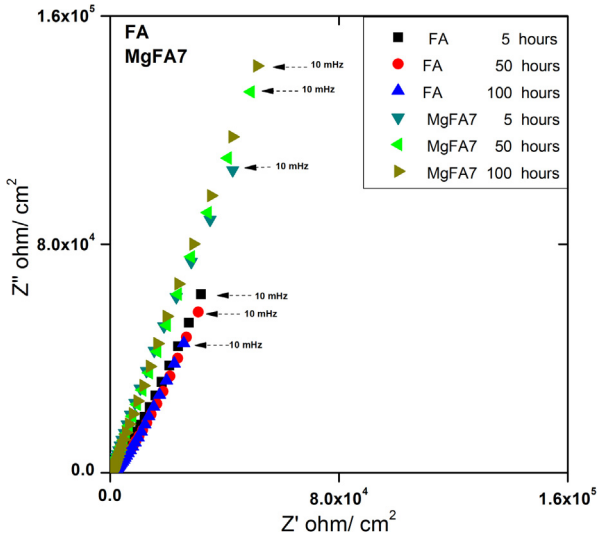


**Fig. 12.** Nyquist plot comparison of fluorapatite (FA) and 7% at. Mg-substituted FA (MgFA7). Coatings up to 100 h of immersion time in Ringer's solution.

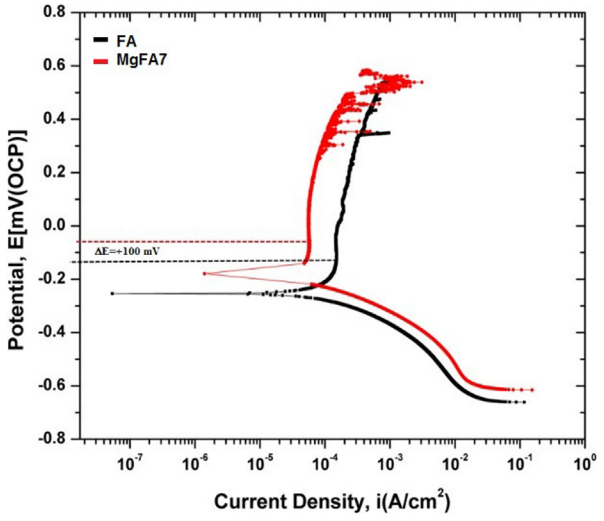


**Fig. 13.** Polarization curves of fluorapatite (FA) and 7% at. Mg-substituted FA (MgFA7) coatings up to 100 h of immersion time in Ringer's solution.

**Table 9**
Corrosion potential ($E_{corr}$) and current densities ($i_{corr}$) at +100 mV of overpotential and start potentials of instabilities in the FA and MgFA7 coatings.

| Sample | $E_{corr}$ (V) | $i_{corr}$ (A·cm$^{-2}$) | $i_{corr}$ (E = +100 mV) | E (V) |
|---|---|---|---|---|
| FA | −0.30 | 120 | 150 | 0.35 |
| MgFA7 | −0.20 | 50 | 60 | 0.25 |

showed in Fig. 11.

For the FA coated substrate (Fig. 10a), a mixed mode fracture was generally observed, involving both a cohesive failure in the adhesive and an interfacial fracture between the coating and the substrate. On the other hand, the MgFA7 coated substrate (Fig. 11b) exhibited a single interfacial fracture mode between the adhesive and the coating. In both cases, failure, either partial or full, was not located at the coating substrate interface, consequently the adhesive strength between coating and substrate could not be determined. However, it corresponds to a value greater than the average adhesive strength. Using the pull-off test method, Sharifnabi et al. [4], stated that the adhesive strength of their sol-gel deposited 10% MgFA coating to a AISI 316L SS stainless steel substrate was greater than 3.7 MPa. Tables 7 and 8 show the pull-out adhesion test results for the FA coated AISI 316L SS substrate and for MgFA7 coated AISI 316L SS substrate, respectively.

**Table 10**
Atomic concentration obtained by XPS to samples FA and MgFA7 after 100 h exposed to Ringer's solution.

| Peak | FA | MgFA7 |
|---|---|---|
| | **at.%** | |
| C 1s | 14.30 | 13.8 |
| Ca 2p | 1.10 | 2.10 |
| Mg 1s | – | 0.80 |
| P 2p | 5.00 | 5.70 |
| O 1s | 46.90 | 50.10 |
| F 1s | 0.50 | 1.00 |
| Fe 2p | 17.80 | 17.10 |
| Mn 2p | 1.20 | – |
| Zn 2p | 1.40 | 2.10 |
| Cl 2p | 3.80 | 1.90 |
| Si 2p | – | – |
| Na 2p | 7.00 | 4.30 |
| K 2p | 1.10 | 1.00 |

From Tables 7 and Table 8, the slightly increased adhesive mean failure value to MgFA7 (4.5 ± 0.2) MPa compared to the FA coatings (4.0 ± 0.2) MPa is attributed to the interface synergism of the coating and substrate. It was also observed a mixed mode failure. The higher mean values of failure limit obtained in this study may be associated with the use of a different CN-Y cyanoacrylate adhesive instead of Loctite 907 [4].

The first observation that can be immediately noticed is that the mean failure strength of the fluorapatite coating is lower than that of the magnesium-doped fluorapatite coating. It is however, important to note that this trend is not statistically significant as the standard deviations overlap. Another critical factor that needs to be accounted for when gauging these results is the failure mode. For the FA coating, interfacial (coating/substrate) failure was observed whereas for the MgFA7 coating, only interfacial (adhesive/coating) failure occurred.

The combination of displaying a slightly higher failure strength whilst also only failing in the interfacial (adhesive/coating) mode, strongly supports the notion that magnesium-doping in the fluorapatite lattice leads to improved bonding and coating adhesion. The reasoning behind this could stem from the thinner nature of the coating compared to its undoped counterpart (discovered in the SEM cross-section imaging), as previous studies have supported [42,36,37].

Nyquist diagram is presented in Fig. 12 for periods of exposure in Ringer's solution corresponding to 5 h, 50 h and 100 h. More capacitive results were associated with the MgFA7 coated samples than the FA coating showing that the first one is more protective than the last one. These results support the polarization curves presented in Fig. 12.

Corrosion characterization in the present study was carried out uniquely to compare the protective effects of the two types of coatings tested in Ringer's solution. The polarization curves for the FA and MgFA7 coated substrates after 100 h of exposure to Ringer's solution are presented in Fig. 13. The results show very similar cathodic behaviour for both types of coatings showing that the cathodic reaction was not significantly affected by the incorporation of Mg into the coating. On the other hand, the anodic polarization curves show that the MgFA7 coating resulted in lower anodic current densities due to a more protective film through which current flow was more difficult comparatively to the FA coating. Interestingly, nobler corrosion potentials were associated to the MgFA7 coating despite of Mg being a highly reducing element. This result suggests that the MgFA7 coating acts as a more protective barrier layer than the FA one.

The corrosion potential, $E_{corr}$, corrosion current density $i_{corr}$, and anodic current densities were estimated at E = +100 mV, that is, at an overpotential of 100 mV, for each of the coating tested in Ringer's

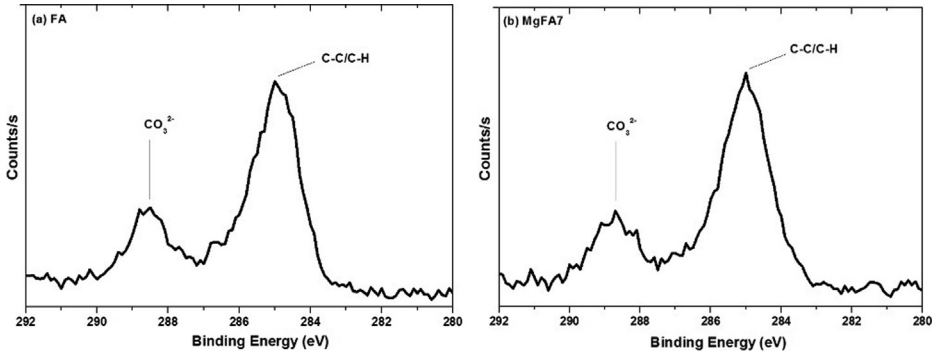


**Fig. 14.** XPS C1s high resolution spectra of (a) fluorapatite (FA) and (b) 7% at. Mg-substituted FA (MgFA7) coatings, after 100 h exposure to Ringer's solution.

**Table 11**
XPS results to C1s high resolution spectra, binding energy, FHWM and atomic concentration to samples FA, and MgFA7 after 100 h exposed to Ringer's solution.

| Sample | **FA** | | **MgFA7** | |
|---|---|---|---|---|
| Peak Fitting | C-C/C-H | $CO_3^{2-}$ | C-C/C-H | $CO_3^{2-}$ |
| BE (eV) | 285.00 | 288.40 | 285.00 | 288.60 |
| FWHM (eV) | 1.69 | 1.74 | 1.74 | 1.76 |
| at.% | 74.80 | 25.20 | 76.30 | 23.70 |

**Table 12**
Atomic concentration obtained by XPS to samples FA and MgFA7.

| Peak | FA | MgFA7 |
|---|---|---|
| | **at.%** | |
| Ca 2p | 13.30 | 13.50 |
| O 1s | 72.00 | 68.60 |
| P 2p | 6.90 | 7.90 |
| Mg 1s | – | 0.90 |
| F 1s | 7.80 | 9.10 |

solution and results are shown in Table 9.

It is worth noticing that at overpotentials of 0.45 mV and 0.65 mV for MgFA7 and FA coated samples, respectively, the current instabilities started, showing that under these conditions the coating becomes unstable.

The stainless-steel samples were exposed to Ringer's solution for different times, along with samples of FA and MgFA7. The compilation of values obtained by XPS results of the corroded area for ten days are shown in Table 10.

**Table 13**
Atomic concentration and binding energy to samples FA and MgFA7.

| Peak fitting | BE (eV) | FA | MgFA7 |
|---|---|---|---|
| | | at.% | |
| $Ca^{2+}$ | 347.6 ± 0.2 | 61.70 | 67.81 |
| Ca-P | 351.0 ± 0.2 | 38.30 | 32.19 |

The exposure of the more active surface of the AISI 316L stainless steel provides the deposition of carbon contaminant and carbonate. The XPS high resolution spectrum for carbon of the samples coatings FA and MgFA7 after 100 h of exposure to Ringer's solution are shown in Fig. 14.

The high values of contaminated carbon are related to activation of the surface by prolonged exposure to the corrosive solution and consequent adsorption of these hydrocarbons by manipulation and exposure to the environment [35]. The atomic concentration values for contaminant carbon and carbonate, the binding energies and FWHM for samples exposed for 100 h the Ringer's solution are shown in the Table 11.

Prior to corrosion, the highest atomic concentration values for C 1s observed were 10.1% and 8% respectively for samples AISI 316L and MgFA6 (Table 1). Compared to these initial values the carbon concentration increased significantly showing that the FA and MgFA7 coatings are susceptible to contamination. After corrosion, the carbonate species are incorporated as gaseous impurities by the process of absorption of atmospheric $CO_2$. According to the initial analysis procedures, removing the representative elements of contamination and of the substrate the elements of interest show agreement with the initial stoichiometries. From XPS results, the atomic concentration values for the elements of interest to samples FA and MgFA7 are shown in

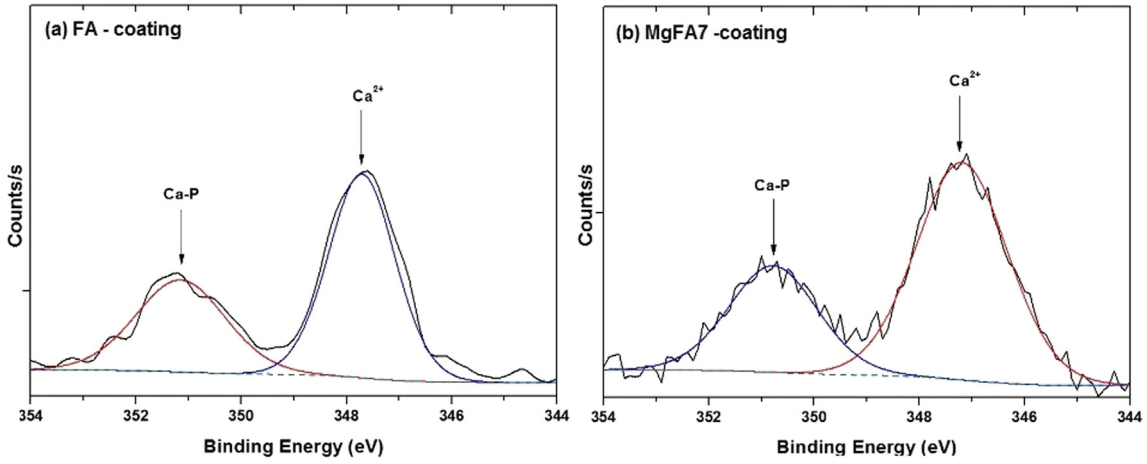


**Fig. 15.** XPS Ca 2p high resolution spectra for (a) fluorapatite (FA) and (b) 7% at. Mg-substituted FA (MgFA7) coating, after 100 h exposure to Ringer's solution.

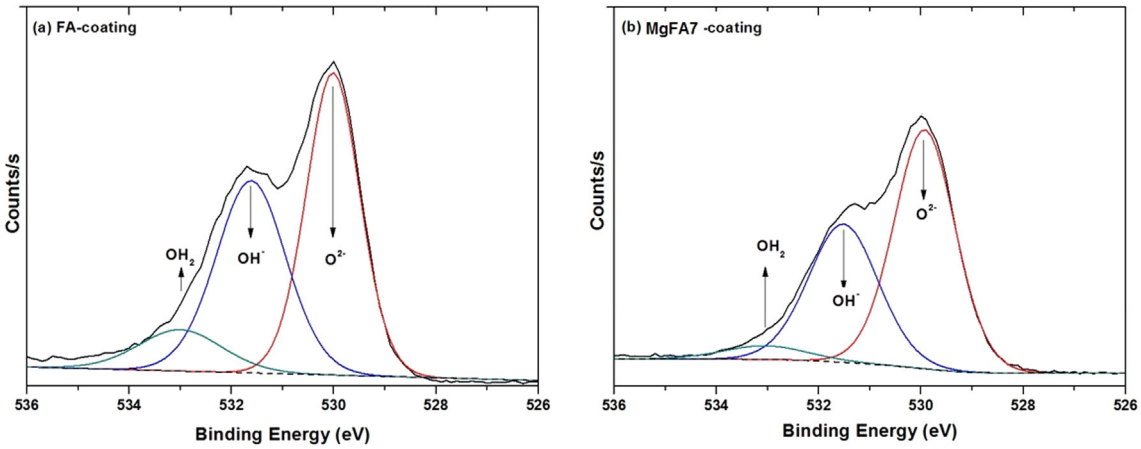


**Fig. 16.** XPS O 1s high resolution spectra to (a) fluorapatite (FA) and (b) 7% at. Mg-substituted FA (MgFA7) coating after 100 h exposure to Ringer's solution.

**Table 14**
Atomic concentration and binding energy for samples fluorapatite (FA) and 7% at. Mg-substituted FA (MgFA7).

| Peak fitting | BE (eV) | FA | MgFA7 |
|---|---|---|---|
| | | at.% | |
| $O_2^-$ | 530.0 ± 0.2 | 49.00 | 57.50 |
| $OH^-$ | 531.5 ± 0.3 | 40.60 | 38.00 |
| $OH_2$ | 533.0 ± 0.2 | 10.40 | 4.50 |

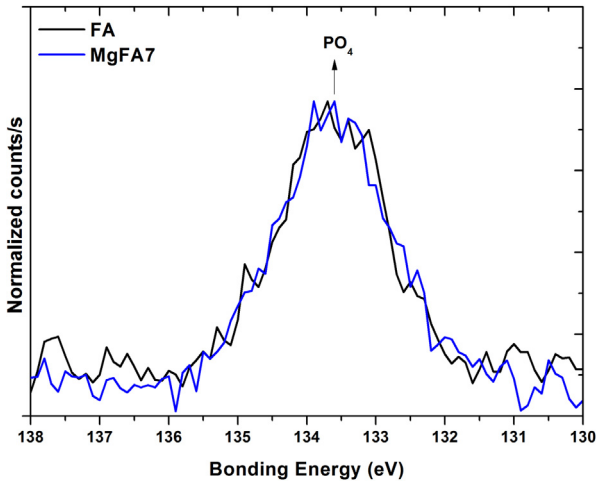


**Fig. 17.** High resolution XPS normalized peaks for P $2p_{3/2}$ for samples fluorapatite (FA) and 7% at. Mg-substituted FA (MgFA7) after 100 h exposure to Ringer's solution.

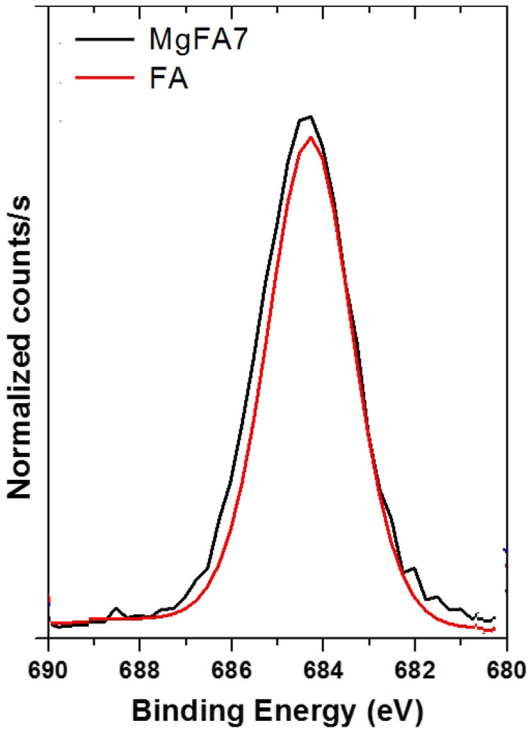


**Fig. 18.** High resolution XPS normalized peaks for F 1 s for samples fluorapatite (FA) and 7% at. Mg-substituted FA (MgFA7) after 100 h exposure to Ringer's solution.

Table 12.

It is also possible to observe that 100 h of exposure in corrosive Ringer's solution is enough to remove part of the layer with the decrease in the concentration of the elements referring to fluorapatite and fluorapatite substituted with 7% of magnesium. The calcium and fluoride contents decrease to the half of uncorroded values to FA and MgFA7 samples and the increase in oxygen concentration is due to carbonates absorbed by corrosion followed by exposure to air.

The XPS results showed that the stoichiometries are different for the coatings FA and that the FA magnesium substituted with magnesium. High exposure times to the corrosive solution containing calcium lead to the solubilization of this coating causing change in the stoichiometry of fluorapatite and fluoroapatite substituted with magnesium. The possibility of deposition of calcium in different chemical forms as oxides was discharged by the results of Ca $2p_{1/2}$ and Ca $2p_{3/2}$ fitting peaks, shown in Fig. 15.

Exposure to corrosive solution, made the XPS calcium peaks high in resolution, become sharper when presenting two peaks Ca $2p_{1/2}$ and Ca $2p_{3/2}$. Although the amount of elements relative to fluorapatite decreased after corrosion, it was observed that for Ca $2p_{3/2}$ increased when compared to unexposed surfaces and increased with magnesium content. The compilation of the XPS results after 100 h on Ringer's solution, atomic concentration and binding energies, Ca $2p_{1/2}$ ($Ca^{2+}$) and Ca $2p_{3/2}$ (Ca-P) peak fitting for coatings FA, and MgFA7 are shown in Table 13.

The XPS high resolution spectrum for O 1s of the coatings FA and MgFA7 after 100 h of exposure to Ringer's solution are shown in Fig. 16.

The XPS O 1s spectrum of FA and MgFA7 coatings contains three oxygen species: $O^{2-}$, $OH^-$ and adsorbed $H_2O$. However, compared to the non-corroded samples (Table 5) the binding energy for these peaks

underwent changes at BE values 530 ± 0.2 eV, 531.5 ± 0.2 eV and 533 ± 0.2 eV. The shape of peaks for samples FA and MgFA7 is similar, the main component at BE = 530 eV can be attributed to $O^{2-}$. For fluorapatite magnesium substituted MgFA7 the main component is the species at BE = 532 eV, attributable to hydroxide. The compilation of XPS results are shown in Table 14.

After 100 h of exposure in Ringer's solution the XPS results for the oxygen peak, show that samples FA and MgFA7 undergo more intense surface oxidation and it may have on its surface the formation of fluor hydroxyapatite (FA). The high resolution XPS normalized peaks for P $2p_{3/2}$ for the coatings samples FA and MgFA7 are shown in Fig. 17.

After 100 h of exposure in Ringer's solution the phosphorus peaks became sharper and the concentrations changed. The shape of the peaks P $2p_{3/2}$ for the same to fluorapatite and fluorapatite substituted with magnesium are similar. The penetration of the electrolyte observed in the electrochemical testing leads to the formation of corrosion products containing calcium, potassium and elements of the corrosive solution, making in this time the clearest fluorapatite layer. The High resolution XPS normalized peaks for F 1s for samples fluorapatite (FA) and 7% at. Mg-substituted FA (MgFA7) after 100 h exposure to Ringer's solution are shown in Fig. 18.

It is possible to observe that when comparing the XPS spectra for F 1s before (Fig. 7) and after corroding (Fig. 18 it is possible to observe that the corrosion removes elements and makes the remaining surface very close to the composition of fluorapatite.

The output of these elements also makes the XPS spectra for F 1s sharper, better resolution and with a narrower shape change. The increase in the atomic concentration of the fluorine element compared to the results obtained prior to corrosion are also evidences of how the surface become less complex than the surfaces of Mg substituted FA resembling the surfaces of FA as obtained.

## 4. Conclusion

In the present work, fluoroapatite and fluoroapatite coatings substituted with magnesium were obtained by the sol gel deposition process on AISI 316 L stainless steel substrate. The X-ray diffraction (XRD) and X-ray photoelectron spectroscopy (XPS) analysis proved that the desired stoichiometries were obtained. Among these stoichiometries the coating with substitution of 7% magnesium presents better resistance to corrosion in simulated body solution and high adhesion on substrate obtained by pull-out adhesion tests. The SEM morphology analysis showed that the addition of magnesium causes a coating densification, with a lower number of defects present in the 7% magnesium substituted comparatively with 6% magnesium substituted fluoroapatite coating. This explains the most capacitive electrochemical results observed for the coating of 7% magnesium substituted fluoroapatite, which acts as a protective barrier. The 100 h of exposure in corrosive Ringer's solution is enough to remove part of the layer with the decrease in the concentration of the elements referring to fluorapatite substituted with 7% of magnesium. The stoichiometries of 5% and 10% of magnesium substituted in fluorapatites reported in the literature showed efficacy in corrosion protection of AISI 316L stainless steel and the results obtained in the present work for intermediate stoichiometries show comparatively potential as corrosion protection coating. Due to this fact the intermediate stoichiometries in 5% and 10% of magnesium substituted in fluorapatites should be investigated for long periods of time and in conditions simulating the human body to be used as coating on medical implants, including osseo bone integration tests.

## Declaration of Competing Interest

The authors declared that there is no conflict of interest.

## Acknowledgements

The authors gratefully acknowledge the Royal Academy of Engineering - Newton Research Collaboration, UK, offering the financial support for this work (Newton Research Collaboration Programme (3)-NRCP1516/1/143). To professor John F. Watts and Steve Hinder from the University of Surrey for teaching and help with XPS results.

## Appendix A. Supplementary material

Supplementary data to this article can be found online at https://doi.org/10.1016/j.apsusc.2019.144393.

## References

[1] M. Bramowicz, L. Braic, F. Ak Azem, S. Kulesza, I. Birlik, A. Vladescu, Mechanical properties and fractal analysis of the surface texture of sputtered hydroxyapatite coatings, Appl. Surf. Sci. 379 (2016) 338–346, https://doi.org/10.1016/j.apsusc.2016.04.077.
[2] Yu. Sirui Li, Yuming Tang Zuo, Xuhui Zhao, The electroplated Pd–Co alloy film on 316L stainless steel and the corrosion resistance in boiling acetic acid and formic acid mixture with stirring, Appl. Surf. Sci. 321 (2014) 179–187, https://doi.org/10.1016/j.apsusc.2014.10.013.
[3] N. Duraipandy, K.M. Syamala, N. Rajendran, Antibacterial effects, biocompatibility and electrochemical behavior of zinc incorporated niobium oxide coating on 316L SS for biomedical applications, Appl. Surf. Sci. 427 (2018) 1166–1181, https://doi.org/10.1016/j.apsusc.2017.08.221.
[4] A. Sharifnabi, M.H. Fathi, B.E. Yekta, M. Hossainalipour, The structural and biocorrosion barrier performance of Mg-substituted fluorapatite coating on 316L stainless steel human body implant, Appl. Surf. Sci. 288 (2014) 331–340, https://doi.org/10.1016/j.apsusc.2013.10.029.
[5] Q. Zhao, Y. Liu, C. Wang, S. Wang, N. Peng, C. Jeynes, Bacterial adhesion on ion-implanted stainless steel surfaces, Appl. Surf. Sci. 253 (21) (2007) 8674–8681, https://doi.org/10.1016/j.apsusc.2007.04.044.
[6] K.P. Ananth, A.J. Nathanael, S.P. Jose, T.H. Oh, D. Mangalaraj, A.M. Ballamurugan, Controlled electrophoretic deposition of HAp/β-TCP composite coatings on piranha treated 316L SS for enhanced mechanical and biological properties, Appl. Surf. Sci. 353 (2015) 189–199, https://doi.org/10.1016/j.apsusc.2015.06.111.
[7] J. Zhao, D. Xu, M.B. Shahzad, Q. Kang, Y. Sun, Z. Sun, K. Yang, Effect of surface passivation on corrosion resistance and antibacterial properties of Cu-bearing 316L stainless steel, Appl. Surf. Sci. 386 (2016) 371–380, https://doi.org/10.1016/j.apsusc.2016.06.036.
[8] L. Wang, X. Zhao, M.H. Ding, H. Zheng, H.S. Zhang, B. Zhang, G.Y. Wu, Surface modification of biomedical AISI 316L stainless steel with zirconium carbonitride coatings, Appl. Surf. Sci. 340 (2015) 113–119, https://doi.org/10.1016/j.apsusc.2015.02.191.
[9] M. Afshar-Mohajer, A. Yaghoubi, S. Ramesh, A.R. Bushroa, K.M.C. Chin, C.C. Tin, W.S. Chiu, Electrophoretic deposition of magnesium silicates on titanium implants: Ion migration and silicide interfaces, Appl. Surf. Sci. 307 (2014) 1–6, https://doi.org/10.1016/j.apsusc.2014.04.033.
[10] M. Dehestani, D. Zemlyanov, E. Adolfsson, L.A. Stanciu, Improving bioactivity of inert bioceramics by a novel Mg-incorporated solution treatment, Appl. Surf. Sci. 425 (2017) 564–575, https://doi.org/10.1016/j.apsusc.2017.07.009.
[11] Z. Dong, J. Chang, Y. Deng, A. Joiner, In vitro remineralization of acid-etched human enamel with $Ca_3SiO_5$, Appl. Surf. Sci. 256 (8) (2010) 2388–2391, https://doi.org/10.1016/j.apsusc.2009.10.072.
[12] G. He, J. Hu, S.C. Wei, J.H. Li, X.H. Liang, E. Luo, Surface modification of titanium by nano-$TiO_2$/HA bioceramic coating, Appl. Surf. Sci. 255 (2) (2008) 442–445, https://doi.org/10.1016/j.apsusc.2008.06.088.
[13] P.R. Prezas, B.M.G. Melo, L.C. Costa, M.A. Valente, M.C. Lança, J.M.G. Ventura, L.F.V. Pinto, M.P.F. Graça, TSDC and impedance spectroscopy measurements on hydroxyapatite, β-tricalcium phosphate and hydroxyapatite/β-tricalcium phosphate biphasic bioceramics, Appl. Surf. Sci. 424 (Part 1) (2017) 28–38, https://doi.org/10.1016/j.apsusc.2017.02.225.
[14] R. Hussain, S. Tabassum, M.A. Gilani, E. Ahmed, A. Sharif, F. Manzoor, S.A. Siddiqi, In situ synthesis of mesoporous polyvinyl alcohol/hydroxyapatite composites for better biomedical coating adhesion, Appl. Surf. Sci. 364 (2016) 117–123, https://doi.org/10.1016/j.apsusc.2015.12.057.
[15] F.V. Anghelina, D.N. Ungureanu, V. Bratu, I.N. Popescu, C.O. Rusanescu, Fine structure analysis of biocompatible ceramic materials based hydroxyapatite and metallic biomaterials 316L, Appl. Surf. Sci. 285 (2013) 65–71, https://doi.org/10.1016/j.apsusc.2013.06.102.
[16] M. Ferri, S. Campisi, M. Scavini, C. Evangelisti, P. Carniti, A. Gervasini, In-depth study of the mechanism of heavy metal trapping on the surface of hydroxyapatite, Appl. Surf. Sci. 475 (2019) 397–409, https://doi.org/10.1016/j.apsusc.2018.12.264.
[17] J.M. Jang, H.C. Choe, W.A. Brantley, Surface observation of nanotube-formed titanium by anodization in electrolyte containing hydroxyapatite nanoparticles, Appl. Surf. Sci. 483 (2019) 76–84, https://doi.org/10.1016/j.apsusc.2019.03.276.
[18] R. Chakraborty, J.S. Manna, D. Das, M. Sen, P. Saha, A comparative outlook of

corrosion behaviour and chlorophyll assisted growth kinetics of various carbon nano-structure reinforced hydroxyapatite-calcium orthophosphate coating synthesized in-situ through pulsed electrochemical deposition, Appl. Surf. Sci. 475 (2019) 28–42, https://doi.org/10.1016/j.apsusc.2018.12.217.

[19] S. Höhn, S. Virtanen, A.R. Boccaccini, Protein adsorption on magnesium and its alloys: a review, Appl. Surf. Sci. 464 (2019) 212–219, https://doi.org/10.1016/j.apsusc.2018.08.173.

[20] K. Ozeki, H. Aoki, T. Masuzawa, Influence of the hydrothermal temperature and pH on the crystallinity of a sputtered hydroxyapatite film, Appl. Surf. Sci. 256 (23) (2010) 7027–7031, https://doi.org/10.1016/j.apsusc.2010.05.018.

[21] R. Kumari, J.D. Majumdar, Studies on corrosion resistance and bio-activity of plasma spray deposited hydroxylapatite (HA) based $TiO_2$ and $ZrO_2$ dispersed composite coatings on titanium alloy (Ti-6Al-4V) and the same after post spray heat treatment, Appl. Surf. Sci. 420 (2017) 935–943, https://doi.org/10.1016/j.apsusc.2017.05.208.

[22] A.A. Ivanova, M.A. Surmeneva, R.A. Surmenev, D. Depla, Structural evolution and growth mechanisms of RF-magnetron sputter-deposited hydroxyapatite thin films on the basis of unified principles, Appl. Surf. Sci. 425 (2017) 497–506, https://doi.org/10.1016/j.apsusc.2017.07.039.

[23] J. Xu, Y. Wang, Y. Huang, H. Cheng, H.J. Seo, Surface reactivity and hydroxyapatite formation on $Ca_5MgSi_3O_{12}$ ceramics in simulated body fluid, Appl. Surf. Sci. 423 (2017) 900–908, https://doi.org/10.1016/j.apsusc.2017.06.268.

[24] Y. Yan, X. Zhang, H. Mao, Y. Huang, Q. Ding, X. Pang, Hydroxyapatite/gelatin functionalized graphene oxide composite coatings deposited on $TiO_2$ nanotube by electrochemical deposition for biomedical applications, Appl. Surf. Sci. 329 (2015) 76–82, https://doi.org/10.1016/j.apsusc.2014.12.115.

[25] D.G. Wang, C.Z. Chen, J. Ma, T. He, Microstructure evolution of sol-gel HA films, Appl. Surf. Sci. 257 (7) (2011) 2592–2598, https://doi.org/10.1016/j.apsusc.2010.10.028.

[26] G. Kačiulis, L. Mattogno, M. Pandolfi, G. Cavalli, A. Gnappi, A. Montenero, XPS study of apatite-based coatings prepared by sol–gel technique, Appl. Surf. Sci. 151 (1–2) (1999) 1–5, https://doi.org/10.1016/S0169-4332(99)00267-6.

[27] J. Zhao, X. Dong, M. Bian, J. Zhao, Y. Zhang, Y. Sun, J. Chen, X. Wang, Solution combustion method for synthesis of nanostructured hydroxyapatite, fluorapatite and chlorapatite, Appl. Surf. Sci. 314 (2014) 1026–1033, https://doi.org/10.1016/j.apsusc.2014.06.075.

[28] H. Agougui, A. Aissa, M. Debbabi, Synthesis and characterization of calcium hydroxy and fluoroapatite functionalized with methyl phosphonic dichloride, Appl. Surf. Sci. 261 (2012) 182–188, https://doi.org/10.1016/j.apsusc.2012.07.136.

[29] Z.L. Zhu, H.Y. Yu, Q. Zeng, H. He, Characterization and biocompatibility of fluoridated iphasic calcium phosphate ceramics, Appl. Surf. Sci. 255 (2) (2008) 552–554, https://doi.org/10.1016/j.apsusc.2008.06.055.

[30] S.T. Jiang, J. Zhang, S.Z. Shun, M.F. Chen, The formation of FHA coating on biodegradable Mg-Zn-Zr alloy using a two-step chemical treatment method, Appl. Surf. Sci. 388 (2016) 424–430, https://doi.org/10.1016/j.apsusc.2015.12.087.

[31] M. Mardali, H.R. SalimiJazi, F. Karimzadeh, B. Luthringer, C. Blawert, S. Labbaf, Comparative study on microstructure and corrosion behavior of nanostructured hydroxyapatite coatings deposited by high velocity oxygen fuel and flame spraying on AZ61 magnesium based substrates, Appl. Surf. Sci. 465 (2019) 614–624, https://doi.org/10.1016/j.apsusc.2018.09.127.

[32] Y. Yajing, D. Qiongqiong, H. Yong, S. Han, X. Pang, Magnesium substituted hydroxyapatite coating on titanium with nanotublar $TiO_2$ intermediate layer via electrochemical deposition, Appl. Surf. Sci. 305 (2014) 77–85, https://doi.org/10.1016/j.apsusc.2014.02.163.

[33] A. Szcześ, Y. Yan, E. Chibowski, L. Hołysz, M. Banach, Properties of natural and synthetic hydroxyapatite and their surface free energy determined by the thin-layer wicking method, Appl. Surf. Sci. 434 (2018) 1232–1238, https://doi.org/10.1016/j.apsusc.2017.11.250.

[34] M. Tavakkoli-Gilavan, H. Abdizadeh, M.R. Golobostanfard, Biomineralization behavior of electrophoretic-deposited hydroxyapatite-tricalcalcium phosphate biphasic composite, Appl. Surf. Sci. 458 (2018) 988–995, https://doi.org/10.1016/j.apsusc.2018.07.168.

[35] J.E. Castle, M.A. Baker, The feasibility of an XPS expert system demonstrated by a rule set for carbon contamination, J. Electron Spectrosc. 105 (2–3) (1999) 245–256, https://doi.org/10.1016/S0368-2048(99)00065-1.

[36] J.E. Castle, Module to guide the expert use of x-ray photoelectron spectroscopy by corrosion scientists, J. Vac. Sci. Technol. A 25 (1) (2007) 1–27, https://doi.org/10.1116/1.2406058.

[37] H.B. Lu, C.T. Campbell, D.J. Graham, B.D. Ratner, Surface characterization of hydroxyapatite and related calcium phosphates by XPS and TOF-SIMS, Anal. Chem. 72 (13) (2000) 2886–2894, https://doi.org/10.1021/ac990812h.

[38] S. Chander, D.W. Fuerstenau, An XPS study of the flouride uptake by hydroxyapatite, Colloids surf. 13 (1985) 137–144, https://doi.org/10.1016/0166-6622(85)80012-3.

[39] B. Demri, D. Muster, XPS study of some calcium compounds, J. Mater. Process. Technol. 55 (3–4) (1995) 311–314, https://doi.org/10.1016/0924-0136(95)02023-3.

[40] T. Hanawa, M. Ota, Calcium phosphate naturally formed on titanium in electrolyte solution, Biomaterials 12 (8) (1991) 767–774, https://doi.org/10.1016/0142-9612(91)90028-9.

[41] T. Hanawa, In vivo metallic biomaterials and surface modification, J. Mater. Sci. Eng. A 267 (2) (1999) 260–266, https://doi.org/10.1016/S0921-5093(99)00101-X.

[42] H. Yong, F. Tao, L. Jian, X. Kewei, Characterization and stability of hydroxyapatite coatings prepared by an electrodeposition and alkaline-treated process, J. Biomed. Mater. Res. A 54 (1) (2000) 96–101, https://doi.org/10.1002/1097-4636(200101)54:13.0.CO;2-U.

[43] Z. Zhang, M.F. Dunn, T.D. Xiao, A.P. Tomsia, E. Saiz, Nanostructured hydroxyapatite coatings for improved adhesion and corrosion resistance for medical implants, MRS Proceedings, vol. 703 (7), Cambridge University Press, 2001, , https://doi.org/10.1557/PROC-703-V7.5.

[44] S. Morais, J.P. Sousa, M.H. Fernandes, G.S. Carvalho, J.D. de Bruijn, C.A. van Blitterswijk, Decreased consumption of Ca and P during in vitro biomineralization and biologically induced deposition of Ni and Cr in presence of stainless steel corrosion products, J. Biomed. Mater. Res. 42 (1998) 192–220, https://doi.org/10.1177/088532829901400202.

[45] B. Aksakal, M. Gavgali, B. Dikici, The effect of coating thickness on corrosion resistance of hydroxyapatite coated Ti6Al4V and 316L SS implants, J. Mater. Eng. Perform. 19 (6) (2010) 894–899, https://doi.org/10.1007/s11665-009-9559-7.

[46] G. Manivasagam, D. Dhinasekaran, A. Rajamanickam, Biomedical implants: corrosion and its prevention – a review, Recent Pat. Corros. Sci. 2 (2010) 40–54, https://doi.org/10.2174/1877610801002010040.